# Millimeter-Wave Heterojunction MITATT Diodes

NUMAN S. DOGAN, MEMBER, IEEE, JACK R. EAST, MEMBER, IEEE, MICHAEL E. ELTA, MEMBER, IEEE, AND GEORGE I. HADDAD, FELLOW, IEEE

*Abstract*—A design theory, a fabrication procedure, and experimental results for heterojunction millimeter-wave transit-time devices operating in the IMPATT (impact ionization avalanche transit-time), MITATT (mixed tunnel-avalanche transit-time), or TUNNETT (tunnel transit-time) mode are presented. An approximate large-signal analysis is developed to investigate the power and efficiency of heterojunction transit-time devices. The results show that significant improvements in efficiency can be achieved by heterojunction structures. The fabrication process developed for the hetrojunction diodes and the millimeter-wave oscillator circuits used in this work are presented. The diodes were operated as oscillators between 65 and 93 GHz. A typical power output of 45 mW at 72 GHz for a 1-percent duty cycle, 1-μs pulse width operation was obtained.

## I. Introduction

THE USE OF transit-time effects to obtain negative resistance was first proposed by Shockley [1] in 1954. Read [2], in 1958, proposed a diode structure in which the negative resistance is caused by a combination of impact avalanche ionization and transit-time effects. The Read diode was successfully fabricated by Lee *et al.* [3] in 1965. At about the same time, a Si p-n junction diode, fabricated by Johnston *et al.* [4], produced microwave oscillations. There has been rapid progress in the two-terminal transit-time device field. The progress achieved to date is due to improvements in material preparation such as molecular beam epitaxy, cicuit design, improved packaging, and heat sink technology and to the development of excellent theoretical models.

Many reasons have been given for the high-frequency limitations of IMPATT mode devices. Skin effect, series resistance, and package effects [5] become very important at high frequencies. The match between the device and circuit impedances becomes increasingly difficult. Diffusion-aided spreading of the injected current pulse [6] and the saturation of the ionization rates at high electric fields [7] will cause a decrease in the device efficiency. Elta and Haddad [8] investigated the frequency limitations of IMPATT, MITATT, and TUNNETT devices and the effects of mixed avalanche and tunneling currents. GaAs IMPATT mode devices were built at 60 GHz with good efficiencies [9]. Above 60 GHz, the performance of GaAs IMPATT diodes has not been investigated in detail. Si IMPATT mode devices have achieved oscillation in a harmonic mode up to 423 GHZ [10]. Although Si IMPATT diodes outperform GaAs IMPATT diodes at high frequencies, they are inherently noisier than GaAs devices.

Incorporating tunneling current into the avalanche breakdown (mixed tunneling and avalanche breakdown) reduces the inherently high noise level in IMPATT diodes. GaAs MITATT diodes also work at higher frequency than GaAs IMPATT diodes. Nishizawa *et al.* [11] obtained oscillations in the 100–248-GHz frequency range from $p^+n^+nn^+$ GaAs diodes with strong tunneling reverse bias characteristics. Elta *et al.* [12] reported oscillations from MITATT GaAs diodes at 150 GHz with 3 mW output power. Work on MITATT and TUNNETT diodes is limited by difficulties in the design and fabrication of these devices. MITATT and TUNNETT diodes are inherently low-negative-resistance diodes, and series resistance further reduces the available negative resistance. Device circuit impedance matching is complicated and difficult to achieve.

Another approach to improving transit-time device operation is velocity modulation. Adlerstein and Chu [9] proposed the DOVETT (double-velocity transit-time) diode to modify the induced current waveform in transit-time devices. The DOVETT has two materials with different saturation velocities in the device drift region. A typical combination would be layers of GaAs and AlGaAs. Depending on the carrier generation mechanism, the DOVETT structures can operate in the IMPATT, MITATT, or TUNNETT mode. An approximate large-signal analysis presented in the following section shows that the dc to RF conversion efficiency of an IMPATT diode cannot be improved very much with velocity modulation since this mode of operation is already inherently efficient. However, the performance of MITATT and TUNNETT diodes can be improved significantly by using double-velocity characteristics.

The remaining sections of this paper will describe the analysis, fabrication, and experimental evaluation of homojunction and heterojunction transit-time devices. An approximate large-signal analysis of the structures is given in Section II. A device fabrication sequence is described in Section III. In Section IV, dc characterization of the devices is described. The millimeter-wave package and test circuit are described in Section V. The RF results are

Manuscript received April 13, 1987; revised August 14, 1987 This work was supported in part by the Naval Research Laboratory.

N S Dogan is with the Department of Electrical Engineering, Washington State University, Pullman, WA.

J R East, M. E. Elta, and G. I. Haddad are with the Center for High-Frequency Microelectronics, Department of Electrical Engineering and Computer Science, University of Michigan, Ann Arbor, MI 48109.

IEEE Log Number 8717393.

0018-9480/87/1200-1308$01.00 ©1987 IEEE

presented in Section VI, and the overall results are summarized in Section VII.

## II. Approximate Analysis

A complete description of transit-time device operation requires a detailed computer simulation of the carrier dynamics and space charge effects. A summary of millimeter IMPATT device properties is given by Mains and Haddad [13]. An approximate large-signal analysis for heterostructure transit-time devices is presented in this section. In the model, the voltage and current waveforms are idealized by assuming saturated velocities and neglecting diffusion to obtain analytic expressions for the power and efficiency. The model can be used to optimize the dimensions and material parameters for a variety of homojunction, single-heterojunction (GaAlAs–GaAs), and double-heterojunction (GaAlAs–GaAs–GaAlAs) structures. The results of the power and efficiency analysis are presented for single- and double-heterojunction structures.

Fig. 1 shows the structure, terminal voltage, injected current, and induced current waveforms for a double-heterojunction transit-time diode. The angles $\theta_m$ and $\theta_\omega$ depend on the injection mechanism. The angle $\theta_m$ is approximately 90° for a tunnel injection process and approximately 180° for an avalanche process. The injection process, in turn, depends on the properties of the generation region and on the operating conditions. The total drift transit angle is denoted by $\theta_d$. Since the induced current is directly proportional to the saturated velocities of the carriers in the drift regions, the current ratio in two different regions can be expressed as

$$\frac{I_2}{I_1} = \frac{\vartheta_{2\text{sat}}}{\vartheta_{1\text{sat}}} = \alpha \tag{1}$$

where $I_2$ and $\vartheta_{2\text{sat}}$ are the current and saturated velocity in region 2 (GaAs) and $I_1$ and $\vartheta_{1\text{sat}}$ are the current and saturated velocity of carriers in region 1 (GaAlAs). The dc current is

$$I_{\text{dc}} = \int_0^{2\pi} I_{\text{ind}}(\omega t)\, d(\omega t) \tag{2}$$

where $I_{\text{ind}}(\omega t)$ is the current induced in the external circuit. Evaluating (2) for the waveforms in Fig. 1 gives

$$I_{\text{dc}} = \frac{1}{2\pi}\left[\frac{\theta_d}{\alpha} + \frac{\alpha+1}{\alpha}\left(\theta_{h_2} - \theta_{h_1}\right)\right] I_1 \tag{3}$$

where $\theta_{h_1}$ and $\theta_{h_2}$ are the injection angles for the first and second heterojunction interfaces, respectively. These junction injection angles are given by

$$\theta_{h_1} = \theta_m - \frac{\theta_\omega}{2} + \omega\tau_{h_1} \tag{4}$$

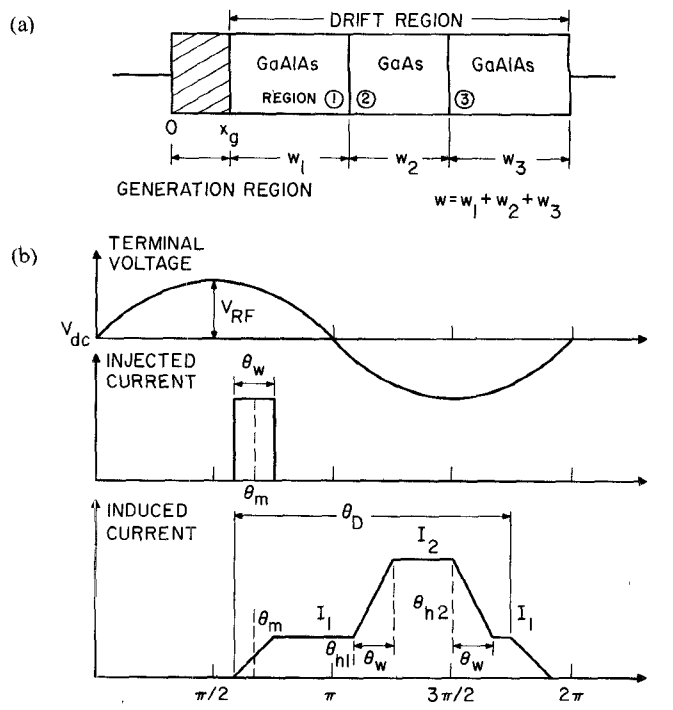


Fig. 1 (a) GaAlAs–GaAs–GaAlAs double-heterojunction two-terminal transit-time device. (b) Terminal voltage, injected current, and induced current for the device.

and

$$\theta_{h_2} = \theta_{h_1} + \omega\tau_{h_2} \tag{5}$$

where $\theta_{h_1}$ and $\theta_{h_2}$ are the transit times in regions 1 and 2, respectively, given by

$$\theta_{h_1} = \frac{W_1}{\vartheta_{1\text{sat}}} \tag{6}$$

and

$$\theta_{h_2} = \frac{W_2}{\vartheta_{2\text{sat}}} \tag{7}$$

where $W_1$ and $W_2$ are the lengths of the GaAlAs (region 1) and the GaAs (region 2) layers, respectively. The efficiency is given by

$$\eta_p = \frac{P_{\text{RF}}}{P_{\text{dc}}} = \frac{V_{\text{RF}}}{V_{\text{dc}}}\eta_n \tag{8}$$

where $P_{\text{RF}}$ is the RF power, $P_{\text{dc}}$ is the dc power, and $\eta_n$ is the normalized efficiency. $P_{\text{RF}}$ and $P_{\text{dc}}$ are given by

$$P_{\text{RF}} = \frac{1}{2\pi}\int_0^{2\pi} I_{\text{ind}}(\omega t) V_{\text{RF}} \sin(\omega t)\, d(\omega t) \tag{9}$$

and

$$P_{\text{dc}} = V_{\text{dc}} I_{\text{dc}}. \tag{10}$$

Evaluating (9) for the waveforms given in Fig. 1 and substituting (3) and (10) into (8) gives

$$\eta_n = \left[\frac{\sin\left(\frac{\theta_\omega}{2}\right)}{\frac{\theta_\omega}{2}}\right] \frac{\frac{1}{\alpha}\left[\cos\theta_m - \cos(\theta_d + \theta_m)\right] + \frac{\alpha-1}{\alpha}\left[\cos\left(\theta_{h_1} + \frac{\theta_\omega}{2}\right) - \cos\left(\theta_{h_2} + \frac{\theta_\omega}{2}\right)\right]}{\frac{\theta_d}{\alpha} + \frac{\alpha-1}{\alpha}\left(\theta_{h_2} - \theta_{h_1}\right)} \tag{11}$$

where $\theta_d$ is the drift transit angle given by

$$\theta_d = \frac{1}{\vartheta_{1\,\mathrm{sat}}}[w_1 + \alpha(w_2 + w_3)]. \tag{12}$$

For a homojunction diode, $\alpha$ is 1 and the familiar equation for a homojunction transit-time device is obtained:

$$\eta_n = \frac{\sin\left(\frac{\theta_\omega}{2}\right)}{\frac{\theta_\omega}{2}}\left[\frac{\cos\theta_m - \cos(\theta_d + \theta_m)}{\theta_d}\right]. \tag{13}$$

The voltage and current waveforms for the single-heterojunction diode are given in Fig. 2. The normalized efficiency can be obtained from the previous results by substituting $\theta_{h_1}$ and $\theta_{h_2}$ as

$$\theta_{h_1} = \theta_h \tag{14}$$

and

$$\theta_{h_2} = \theta_d + \theta_m - \frac{\theta_\omega}{2}. \tag{15}$$

The normalized efficiency of a single-heterojunction diode is obtained by substituting (14) and (15) into (11):

$$\eta_n = \left[\frac{\sin\left(\frac{\theta_\omega}{2}\right)}{\frac{\theta_\omega}{2}}\right] \cdot \frac{\frac{1}{\alpha}\cos\theta_m - \cos(\theta_d + \theta_m) + \frac{\alpha - 1}{\alpha}\cos\left(\theta_h + \frac{\theta_\omega}{2}\right)}{\frac{1-\alpha}{\alpha}\left(\theta_h + \frac{\theta_\omega}{2} - \theta_m\right) + \theta_d} \tag{16}$$

where

$$\theta_h = \theta_m - \frac{\theta_\omega}{2} + \omega\frac{w_1}{\vartheta_{1\,\mathrm{sat}}} \tag{17}$$

and

$$\theta_d = \frac{1}{\vartheta_{1\,\mathrm{sat}}}\left(\omega + \frac{w_2}{\alpha}\omega\right). \tag{18}$$

A computer program to calculate the optimum angles and the corresponding maximum efficiency was written. Since the injection angle $\theta_m$ and the pulse width $\theta_\omega$ are constant for a given device and operating condition, the device structure variables $\theta_{h_1}$, $\theta_{h_2}$, and $\theta_d$ can be chosen to maximize the efficiency. The computer program calculates the optimum angles and the corresponding maximum efficiency using the conjugate gradient method developed by Fletcher and Reeves [14]. Table I gives the numerical results for TUNNETT, MITATT, an IMPATT heterojunction diodes obtained from the computer program. The results show that the efficiency for MITATT and TUNNETT diodes can be improved significantly if heterojunction diodes are used. The first set of data in Table I is

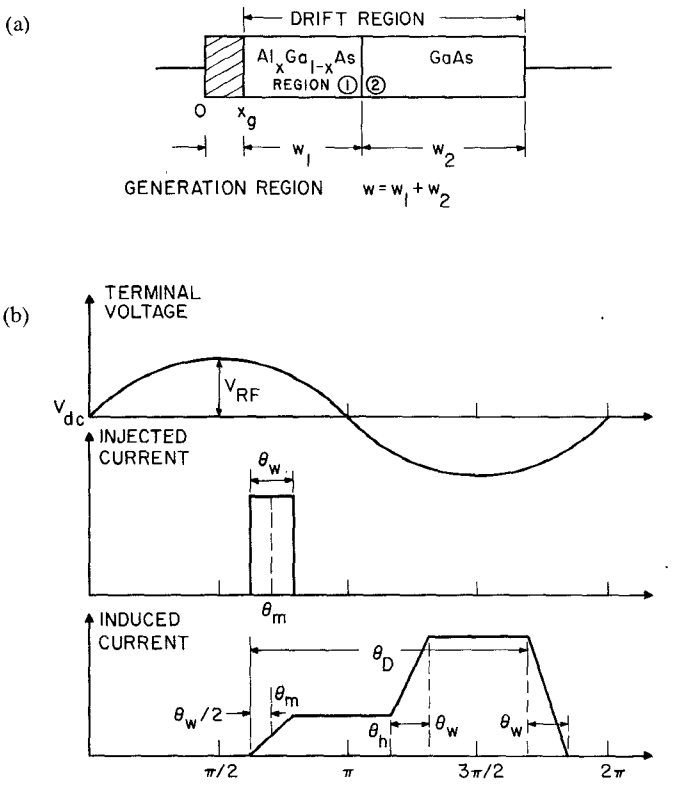


Fig. 2. (a) GaAlAs–GaAs heterojunction two-terminal transit-time device. (b) Terminal voltage, injection current, and induced current for the device in (a), respectively ($\alpha = 3$).

for the idealized case where $\theta_\omega$, the pulse width, is assumed to be zero. In the second set of data, the injection angles and pulse widths are taken from Elta and Haddad [8]. The relative efficiency improvement is calculated as

$$\eta_{\mathrm{rel}} = \frac{\eta_{\mathrm{hetero}} - \eta_{\mathrm{homo}}}{\eta_{\mathrm{homo}}} \tag{19}$$

where $\eta_{\mathrm{hetero}}$ and $\eta_{\mathrm{homo}}$ are the normalized efficiencies of the heterojunction and homojunction transit-time devices, respectively. A heterojunction TUNNETT operating at 100 GHz would have a relative efficiency improvement of 83 percent. The efficiency is almost doubled for $\alpha = 3$. The difference between the maximum power efficiencies of single- and double-heterojunction TUNNETT's is small, which suggests that there would not be much improvement in efficiency by using double-heterojunction over single-heterojunction devices. The numerical results presented in Table I can be used as a guideline for the design of heterojunction devices.

## III. Device Fabrication

Most of the problems associated with the fabrication of high-frequency IMPATT diodes are related to their small size. The active layer thicknesses are reduced for millimeter-wave diodes due to the short transit time at these frequencies. The diode area is also reduced to maintain reasonable impedance levels. Due to the skin effect and parasitic resistance limitations, the required GaAs layer thickness for millimeter-wave IMPATT diodes is typically

TABLE I
NUMERICAL RESULTS FOR TUNNETT, MITATT, AND IMPATT HETEROJUNCTION DIODES

| | Frequency (GHz) | Diode Mode | Injection Angle $\theta_m$ (Degrees) | Pulse Width $\theta_w$ (Degrees) | Drift Angle $\theta_D$ (Degrees) | Junction Angle $\theta_h$ (Degrees) | Normalized Efficiency $\alpha = 3$ (Heterojunction) | Normalized Efficiency $\alpha = 1$ (Homojunction) | Relative Efficiency Improvement Over Homojunction (Percent) |
|---|---|---|---|---|---|---|---|---|---|
| $\alpha$=1 | Ideal | IMPATT | 180.00 | 0 | 133.5626 | -- | -- | - 0.7246 | 15 |
| $\alpha$=3 | Ideal | IMPATT | 180.00 | 0 | 123.2198 | 236.7503 | - 0.8366 | -- | |
| $\alpha$=1 | Ideal | TUNNETT | 90.00 | 0 | 257.4526 | -- | -- | - 0.2172 | 138 |
| $\alpha$=3 | Ideal | TUNNETT | 90.00 | 0 | 238.8700 | 211.1002 | - 0.5170 | -- | |
| $\alpha$=1 | Ideal | MITATT | 135.00 | 0 | 197.4531 | -- | -- | - 0.4625 | 46 |
| $\alpha$=3 | Ideal | MITATT | 135.00 | 0 | 182.4843 | 222.4858 | - 0.6758 | -- | |
| $\alpha$=1 | 10 | IMPATT* | 180.00 | 75.0 | 133.5626 | -- | -- | - 0.6740 | 15 |
| $\alpha$=3 | 10 | IMPATT* | 180.00 | 75.0 | 123.2198 | 199.2790 | - 0.7781 | -- | |
| $\alpha$=1 | 100 | TUNNETT* | 110.1509 | 75.0 | 231.1745 | -- | -- | - 0.2978 | 83 |
| $\alpha$=3 | 100 | TUNNETT* | 110.1509 | 75.0 | 214.0381 | 178.3098 | - 0.5442 | -- | |
| $\alpha$=1 | 100 | MITATT* | 164.8453 | 93.0023 | 155.4120 | -- | -- | - 0.5714 | 25 |
| $\alpha$=3 | 100 | MITATT* | 164.8453 | 93.0023 | 143.4385 | 185.2138 | - 0.7016 | -- | |
| $\alpha$=1 | 100 | IMPATT* | 180.00 | | 134.0114 | -- | -- | - 0.4982 | 35 |
| $\alpha$=3 | 100 | IMPATT* | 180.00 | | 103.2965 | 222.1783 | - 0.6714 | -- | |

*Data taken from Elta [8].

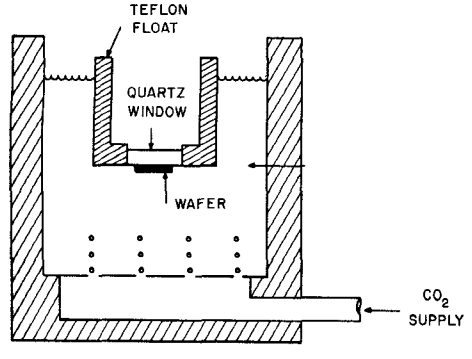


Fig. 3. Cross-sectional drawing of the apparatus used for GaAs etching.

2 to 7 $\mu$m. The GaAs wafer must be thinned from 300 to 400 $\mu$m. Most common methods for thinning GaAs wafers reported in the literature use mechanical abrasion. In this method, wafers are mounted on a lapping fixture and lapped with a compound (commercial microgrit). This lapping and mounting process is repeated and wafer thickness uniformity is checked each time. To obtain better uniformity, as many as five to ten lapping and dismounting steps are needed. This method has several disadvantages. The lapping and dismounting is tedious. The GaAs wafer develops cracks and surface damage that are detrimental to the following processing steps and result in poor electrical characteristics. Due to these limitations, wafer thinning by lapping is limited to diodes where the GaAs layer thickness is greater than 7 to 10 $\mu$m. A wafer thinning and device fabrication process that eliminates most of these problems is described in the remaining portion of this section.

The wafer thinning and fabrication process has three main steps. Since most MBE-grown GaAs wafers are mounted with indium during epitaxial growth, their back sides are covered by indium. The first step is to remove the indium in HCL. However, the indium reacts with GaAs and remains on some portions of the surface. Complete removal of the indium was not possible by chemical etching. Therefore, the remaining indium was removed by lapping the back surface briefly. The damage caused during lapping was removed by polishing the surface on a polishing wheel using 5 percent chlorine bleach and 95 percent DI water. After chemical mechanical polishing, the GaAs surface is shiny and mirror smooth. Brief lapping and chemical–mechanical polishing of the back surface removes only 50 to 75 $\mu$m of GaAs.

The second step is to remove most of the remaining GaAs by chemical bubble etching. A cross-sectional drawing of this apparatus is given in Fig. 3. In this process, $CO_2$ gas is bubbled up through the etching solution providing random agitation of the solution. The wafer to be thinned is mounted on a Teflon cup using paraffin wax. The Teflon cup moves randomly during etching, floating in the solution, and the rising bubbles impinge upon the wafer surface. A solution of $H_2SO_4$:$H_2O_2$:$H_2O$ (1:8:1 volume ratio) was used as an etchant. This provided a fast etch rate (25 $\mu$m/min), uniform wafer thinning, and excellent surface quality. The etch rate and surface quality do not depend on the doping concentration or dopant. Both

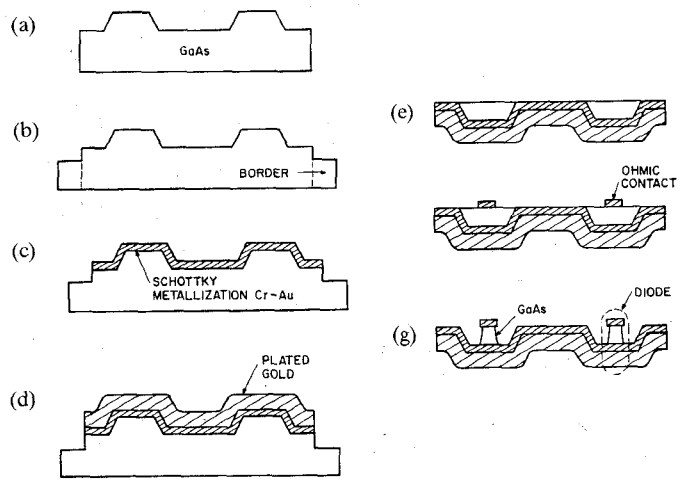


Fig. 4. Two-terminal heterojunction device fabrication process. (a) Mesa etch. (b) Border (rim) etch. (c) Schottky contact metallization. (d) Gold heat sink plating. (e) Slow back side etch until metallization is seen. (f) Ohmic contact. (g) Diode is complete after mesa etch.

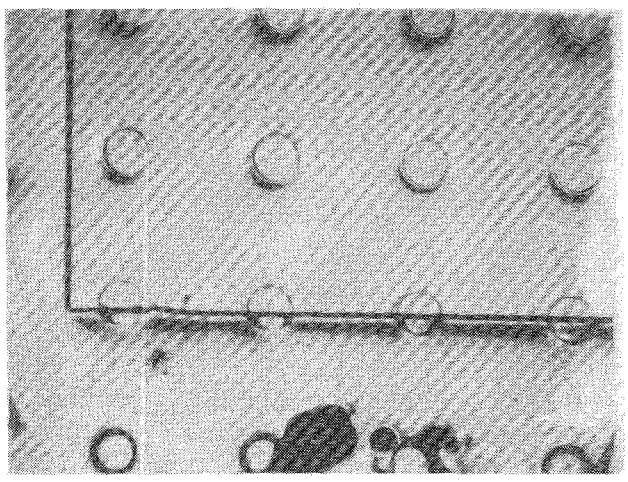

Fig. 5. Border (rim) etch. Border etch is 8 $\mu$m and mesa is 5 $\mu$m (50X magnification).

$n^+$ and semi-insulating wafers were etched and no differences in the etching characteristics were observed.

The third step is to use a series of etching and metallization steps to define the final diode structure. The fabrication sequence is: (a) mesa etching, (b) rim etching, (c) Schottky contact metallization, (d) heat sink plating, (e) back side etching, (f) ohmic contact metallization, and (g) final mesa etching. Fig. 4 shows these processing steps. The final Schottky barrier device contacts will be on the top side of the wafer as shown in Fig. 4(a). Steps (a) and (b) form mesas and a rim on the epitaxial side of the semiconductor wafer. These two depth stops will be used in step (e) as a thickness gauge and etch stop when the final device thickness is obtained. The wafer is mounted on a glass slide that protects the substrate side of the wafer. Using photoresist as a mask, mesas are etched on the epitaxial side of the wafer. The mesa height is the desired final device thickness, and the mesa diameter is approximately 150 $\mu$m. A second photoresist step and etch are used to define a rim or border around the wafer. The rim etch is approximately 3 $\mu$m deep. Both etches use $HCl:H_2O_2:H_2O$ (80:4:1). Fig. 5 shows a photograph of the wafer after steps (a) and (b).

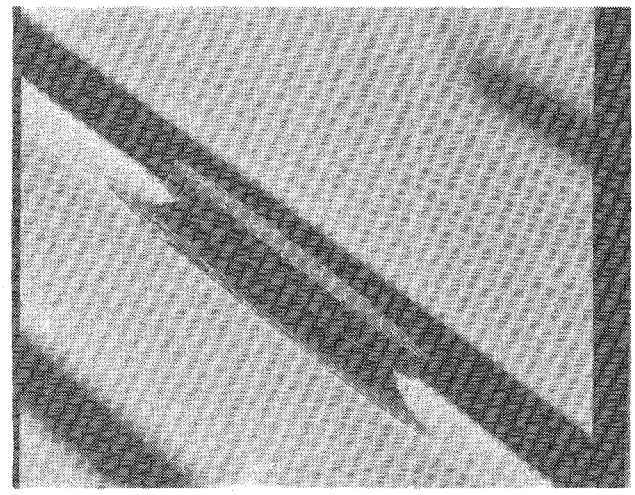

Fig. 6. Heterojunction $GaAs/Ga_{0.6}Al_{0.4}AS$ millimeter-wave diode. Diameter is 0.0015 inch.

Steps (c) and (d) are the Schottky barrier and heat sink formation. The photoresist is removed and the wafer is cleaned. Ti and Au are evaporated over the entire surface except the rim area, and the heat sink metal is electroplated. Two plated heat sink techniques were used. The first technique used electroplated gold approximately 50 $\mu$m thick over the entire wafer. The individual diodes were separated by dicing or chemical etching after the final diode fabrication. The second method used selective heat sink plating. Gold and silver were plated through a photoresist mask to form the final heat sink pattern. This second technique is more complex but allows an easier final diode separation.

Steps (e), (f), and (g) are used to form the final diode structure. The wafer is removed from its supporting glass carrier and remounted with the substrate side of the wafer exposed. The wafer is etched using the bubbler and solution described previously until the rim formed in step (b) is exposed. The rim is used to gauge the remaining thickness of the GaAs wafer. Etching is continued in a solution of $H_2SO_4:H_2O_2:H_2O$ (5:1:1 volume ratio) that has a slow etch rate. As the GaAs mesa pockets are exposed, they are protected with wax. This wax cover and etch process is repeated until all the GaAs pockets are exposed. The final device thickness is the same as the mesa height formed in step (a). After the wafer thinning, AuGe–Ni–Au ohmic contacts are formed and a final mesa etching or proton isolation is performed to define the final device size. Fig. 6 shows a scanning electron microscope photograph of a fabricated GaAs diode. A series of these devices was fabricated and evaluated for their RF performance.

## IV. DC Device Characteristics

A range of device operation from avalanche to tunnel injection is possible in transit-time devices. The injection conditions depend on the properties of the carrier

TABLE II
INITIAL DOPING AND MATERIAL PROFILE

| Layer | Material | Thickness | Doping ($cm^{-3}$) |
|---|---|---|---|
| 1 | GaAs | 1500 Å | $1 \times 10^{18}$ |
| 2 | $Ga_{0.6}Al_{0.4}As$ | 825 Å | $4 \times 10^{16}$ |
| 3 | GaAs | 2500 Å | $4 \times 10^{16}$ |
| 4 | GaAs | 5000 Å | $1 \times 10^{18}$ (buffer) |

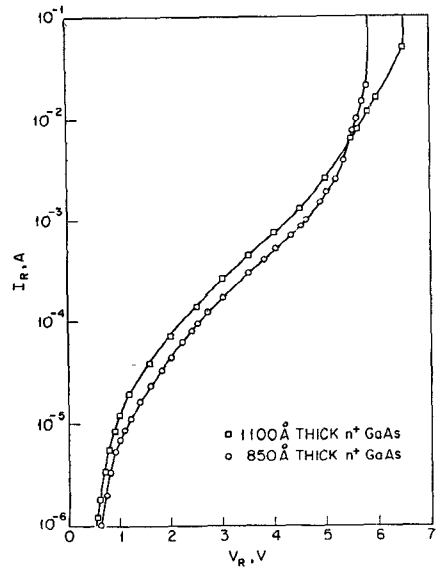


Fig. 7. Device current–voltage characteristics.

generation region of the device. These properties, in turn, depend on the structure, temperature, and bias conditions in the device. Prior to the fabrication of the devices, a series of measurements were made on an MBE-grown test wafer with the structure and doping profile shown in Table II. Using PA11 ($NH_4OH:H_2O_2:H_2O$) as an etchant, layer 1 in Table II was etched on different portions of the wafer to a final thickness ranging from 200 to 1100 Å. The etched layer thicknesses were found by measuring the etch steps with a Dektek. In some portions of the wafer, the first GaAs layer was removed completely, and a small portion of the AlGaAs was removed. Diodes from these different regions were probed and the electrical characteristics were obtained. The information gained from these diode characteristics was used in the design of the heterojunction MITATT diodes that worked successfully.

Fig. 7 shows the reverse bias $I$–$V$ characteristics of devices with layer 1 thicknesses of 1100 and 850 Å. The applied voltage required to extend the depletion layer to the interface between the GaAs and the AlGaAs is 14 V for the 1100-Å-thick layer and 10 V for the 1000-Å-thick layer. Since the voltages in Fig. 7 are lower, the devices are breaking down before punching through to the drift region.

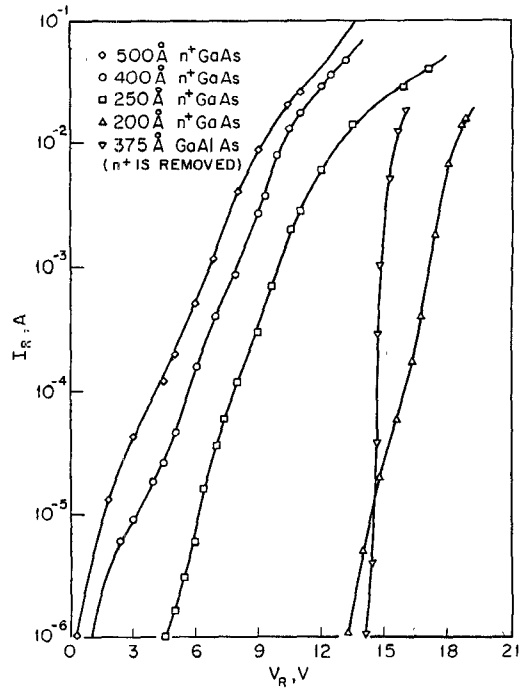


Fig. 8 Device current–voltage characteristic with thinner AlGaAs layer.

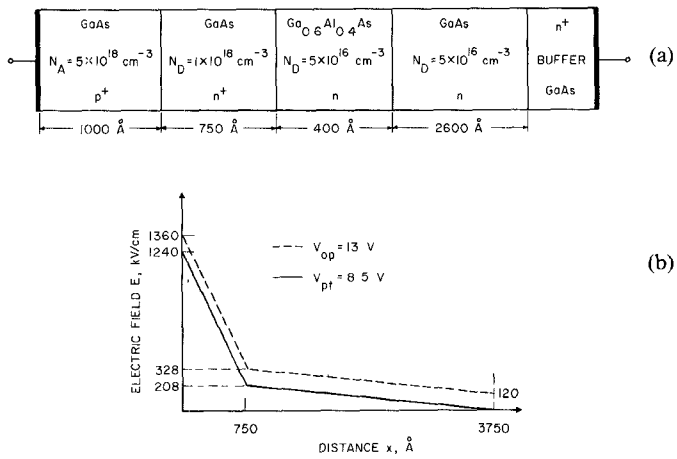


Fig. 9. Diode structure.

Fig. 8 shows the reverse bias $I$–$V$ characteristics of the heterojunction diodes from other regions of the test wafer. For low to moderate reverse bias voltages, the reverse bias current is due to tunneling. For large reverse bias voltages, the reverse bias current is due to avalanche breakdown. The breakdown voltage increases gradually as the $n^+$ region thickness decreases for a fixed reverse bias current.

It is clear from these results that the thickness of the $n^+$ GaAs layer must be chosen carefully for the design of mixed tunnel-avalanche transit-time devices. Using the information obtained from the test sample, a $p^+n^+$ heterojunction diode with the doping profile shown in Fig. 9(a) was designed, and the structure was grown on an $n^+$ GaAs substrate by molecular beam epitaxy. The punch-through voltage for this structure is 8.5 V. The typical operating voltage for the diode is approximately 13 V at 200 mA bias current. The electric field profiles for the

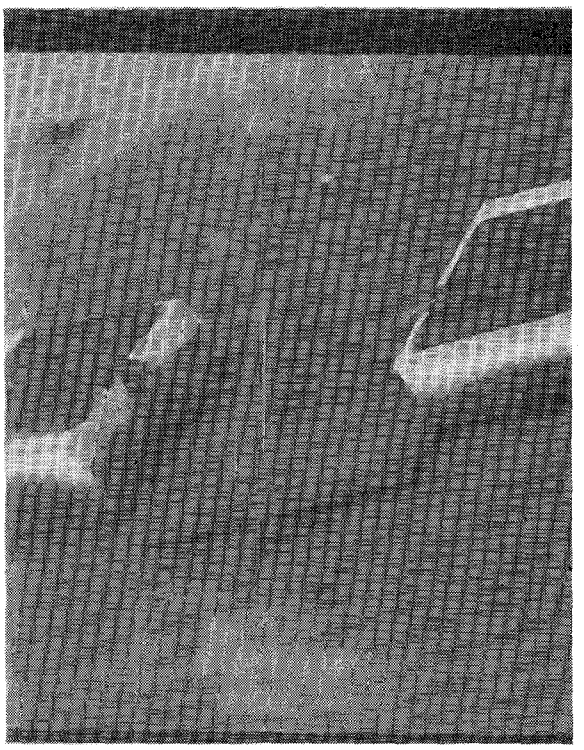

Fig. 10. Scanning electron microscope (SEM) photograph of double-quartz-standoff IMPATT diode for 60-GHz operation. Gold bonding wire is 0.0007 inch in diameter (140× magnification).

punch-through and operating voltages are shown in Fig. 9(b). The zero position of Fig. 9(b) is at the $p^+n^+$ interface in Fig. 9(a). The maximum electric fields on the $p^+n^+$ junction interface are $1.24\times10^6$ V/cm and $1.36\times10^6$ V/cm for $V_{pt}=8.5$ V and $V_{op}=13$ V, respectively.

## V. Packaging, Oscillator Circuit Design, and RF Results

The device package and the oscillator circuit play a critical part in the device performance. Since the package acts as part of the oscillator circuit in millimeter-wave operation, it is important to have low parasitic package elements for better impedance matching between the circuit and the diode. Initially, ceramic commercial packages were used for the device packaging. Difficulties in working with this package and large lead inductances and package parasitic capacitances yielded poor RF performance. Quartz standoffs were then fabricated and used for packaging of millimeter-wave diodes. The RF results reported in this work were obtained with double-quartz standoffs. The standoffs were mounted on both sides of the diode chip and a 0.0007-inch-diameter wire was bonded to the quartz standoffs and the diode. Fig. 10 shows a scanning electron microscope photograph of the double-quartz standoff package.

A top hat resonator waveguide circuit was used for the RF measurements. The circuit utilizes a radial choke in the dc bias port for an RF termination. To obtain better mechanical performance and flexibility, the circuit employs a precision bellows to minimize the force on the quartz standoff. This allows the testing of these fragile structures. The dimensions of the radial choke and the quarter-wave section of the coaxial line were chosen for a 60-GHz operating frequency. The coaxial line above the radial choke was terminated by a tapered lossy material. Fig. 11 shows the $V$-band oscillator circuit in unassembled form.

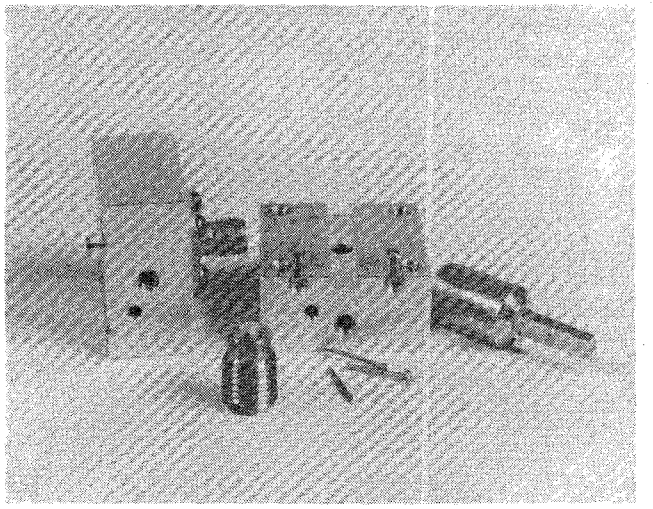

Fig. 11. The $V$-band oscillator circuit. The OSM connector, disk resonators, bias post, diode mounting piece, and back short are shown in the photograph.

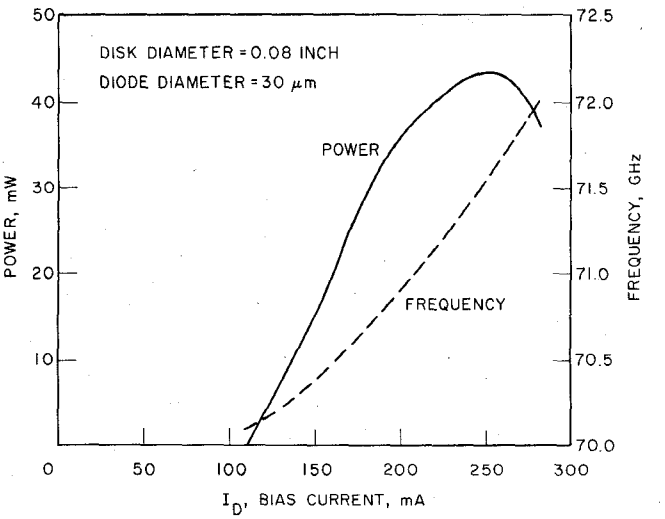


Fig. 12. Device performance.

The MITATT devices were tested using 1 percent duty cycle, 1-μs pulsed operation. The RF performance of the heterostructure MITATT devices is shown in Fig. 12. The measurement system used in this work includes an $E-H$ tuner, a variable attenuator, a wavemeter, a power detector, and a power meter. The best performance was obtained from a 35-μm-diameter diode tested with a 0.1-inch-diameter disk resonator.

## VI. Conclusions

An approximate large-signal design theory, fabrication techniques, and experimental results for millimeter-wave transit-time devices were described. The approximate

large-signal analysis was used to investigate the power and efficiency of heterojunction and transit-time devices. The analysis results show that significant improvement can be achieved for MITATT and TUNNETT devices by using heterostructures for velocity modulation. A device fabrication process that employs a novel wafer-thinning technique was presented in detail. This technique allowed the fabrication of millimeter-wave diodes with GaAs thickness of 1.5 $\mu$m with excellent yield. Both double-drift GaAs IMPATT and heterojunction MITATT diodes were fabricated and their RF performances were presented. Comparable RF performances were obtained for MITATT and double-drift IMPATT devices. The results presented here are preliminary. With better circuit design and doping profile optimization, much better RF performance is expected. However, this is the first time that significant power outputs have been obtained from heterojunction diodes and these results clearly indicate their potential.

## ACKNOWLEDGMENT

The authors would like to thank Dr. H. Morkoc for supplying the MBE wafers used in this work.

## REFERENCES

[1] W. Shockley, "Negative resistance arising from transit time in semiconductor diodes," *Bell Syst. Tech. J.*, vol. 33, no. 4, pp. 799–826, July 1954.
[2] W. J. Read, "A proposed high frequency negative resistance diode," *Bell Syst. Tech. J.*, vol. 37, no. 2, pp. 401–446, Mar. 1958.
[3] C. A. Lee, R. L. Batdorf, W. Weigmann, and G. Kaminsky, "The Read diode—An avalanching, transit-time, negative-resistance oscillator," *Appl. Phys. Lett.*, vol. 6, no. 5, pp. 89–91, Mar. 1, 1965.
[4] R. L. Johnston, B. C. DeLoach, Jr., and B. G. Cohen, "A silicon diode microwave oscillator," *Bell Syst. Tech. J.*, vol. 44, no. 2, pp. 369–372, Feb. 1965.
[5] B. C. DeLoach, Jr., "Thin skin IMPATT's," *IEEE Trans. Microwave Theory Tech.*, vol. MTT-18, pp. 72–74, Jan. 1970.
[6] M. S. Gupta, "A simple approximate method of estimating the effect of carrier diffusion in IMPATT diodes," *Solid-State Electron.*, vol. 18, pp. 327–330, 1975.
[7] T. Misawa, "High-frequency fall-off of IMPATT diode efficiency," *Solid-State Electron.*, vol. 15, pp. 457–465, 1972.
[8] M. E. Elta and G. I. Haddad, "High-Frequency limitations of IMPATT, MITATT, and TUNNETT mode devices," *IEEE Trans. Microwave Theory Tech.*, vol. MTT-27, pp. 442–449, May 1979.
[9] M. G. Adlerstein and S. L. G. Chu, "GaAs IMPATT diodes for 60 GHz," *IEEE Electron Device Lett.*, vol. ELD-5, pp. 97–98, Mar. 1984.
[10] M. Ohmori, T. Ishibashi, and S. Ono, "Dependency of the highest harmonic oscillation frequency on junction diameter of IMPATT diodes," *IEEE Trans. Electron Devices*, vol. ED-24, pp. 1323–1329, Dec. 1977.
[11] J. Nishizawa, K. Motoya, and Y. Okuno, "GaAs TUNNETT diodes," *IEEE Trans. Microwave Theory Tech.* vol. MTT-20, pp. 1029–1035, Dec. 1978.
[12] M. E. Elta, H. R. Fetterman, W. V. Macropoulos, and J. J. Lambert, "150 GHz GaAs MITATT source," *IEEE Electron Device Lett.*, vol. EDL-1, pp. 115–116, June 1980.
[13] R. K. Mains and G. I. Haddad, "Properties and capabilities of millimeter-wave IMPATT diodes," in *Infrared and Millimeter-Waves*, K. J. Buttom, Ed. New York: Academic Press, 1983, part III, ch. 3.
[14] R. Fletcher and C. M. Reeves, "Function minimization by conjugate gradients," *Computer J.*, vol. 7, no. 2, pp. 149–154, 1964.

**Numan S. Dogan** (S'78–M'86) was born in Tokat, Turkey, on January 2, 1955. He received the B.S. degree from the Karadeniz Technical University, Trabzon, Turkey, in 1975, the M.S. degree from the Polytechnic Institute of New York, New York, in 1979, and the Ph.D. degree from the University of Michigan, Ann Arbor, in 1986, all in electrical engineering.

From 1975 to 1977 he worked for the National Power Company of Turkey as an electronics engineer. During his graduate studies at the University of Michigan, he worked as a Teaching and Research Assistant. He is currently an Assistant Professor in the Department of Electrical and Computer Engineering, Washington State University, Pullman. His present research activities involve microwave solid-state devices and circuits.

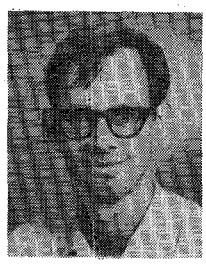

**Jack R. East** (S'70–M'72) obtained the B.S.E., M.S., and Ph.D. degrees from the University of Michigan. He is now an associate research scientist in the Solid-State Electronics Laboratory of the University of Michigan, working in the area of microwave and millimeter-wave solid-state devices.

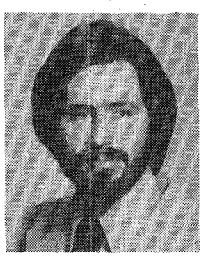

**Michael E. Elta** (S'75–M'78) was born in Flint, MI, on January 1, 1951. He received the B.S.E. degree in electrical engineering from the General Motors Institute, Flint, MI, in 1975 and the M.S.E. degree in electrical engineering from the University of Michigan, Ann Arbor, in 1975. He completed a dissertation for the Ph.D. degree in electrical engineering at the University of Michigan, Ann Arbor, in 1978.

From 1969 to 1973 he was a cooperative engineering student at AC Spark Plug, GMC, Flint, MI; at the University of Michigan, he was a Research Assistant in the Electron Physics Laboratory from 1975 to 1978. From 1978 to 1982 he was a member of the research staff in the microelectronics group at MIT Lincoln Laboratory, Lexington, MA. At present, he is the Manager of the Solid-State Electronics Laboratory in the Electrical Engineering and Computer Science Department at the University of Michigan, Ann Arbor. His research interests include semiconductor device physics, microelectronic fabrication, process modeling, and microwave device design. Dr. Elta is a member of the Tau Beta Phi, Sigma Xi, and the American Vacuum Society.

**George I. Haddad** (S'57–M'61–SM'66–F'72) received the B.S.E., M.S.E., and Ph.D. degrees in electrical engineering from the University of Michigan.

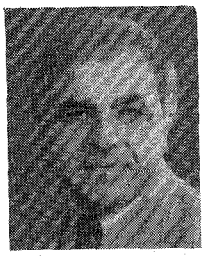

From 1957 to 1958 he was associated with the Engineering Research Institute of the University of Michigan, where he was engaged in research on electromagnetic accelerators. In 1958 he joined the Electron Physics Laboratory. From 1960 to 1969 he served successively as Instructor, Assistant Professor, Associate Professor, and Professor in the Electrical Engineering Department. He served as Director of the Electron Physics Laboratory from 1968 to 1975. From 1975 to 1987 Dr. Haddad served as Chairman of the Department of Electrical Engineering and Computer Science. He is currently Director of both the Solid-State Electronics Laboratory and the Center for High-Frequency Microelectronics. His current research areas are microwave and millimeter-wave solid-state devices and monolithic integrated circuits.

Dr. Haddad received the 1970 Curtis W. McGraw Research Award of the American Society for Engineering Education for outstanding achievements by an engineering teacher, The College of Engineering Excellence in Research Award (1985), and The Distinguished Faculty Achievement Award (1986) of the University of Michigan. He is a member of Eta Kappa Nu, Sigma Xi, Phi Kappa Phi, Tau Beta Pi, and the American Society for Engineering Education.